Precise measurement of the thermal and stellar ^{54}Fe$(n,\gamma)^{55}$Fe cross sections via accelerator mass spectrometry

A. Wallner,[1,2,*] K. Buczak,[2] T. Belgya,[3] M. Bichler,[4] L. Coquard,[5] I. Dillmann,[5,†] R. Golser,[2] F. Käppeler,[5] A. Karakas,[6,7] W. Kutschera,[2] C. Lederer,[2,8] A. Mengoni,[9] M. Pignatari,[10,‡] A. Priller,[2] R. Reifarth,[11] P. Steier,[2] and L. Szentmiklosi[3]

[1]*Department of Nuclear Physics, Research School of Physics and Engineering, The Australian National University, Canberra, ACT 2601, Australia*

[2]*VERA Laboratory, Faculty of Physics, University of Vienna, Austria*

[3]*Nuclear Analysis and Radiography Department, Institute for Energy Security and Environmental Safety, Centre for Energy Research, Hungarian Academy of Sciences, Hungary*

[4]*Atominstitut, Vienna University of Technology, Austria*

[5]*Karlsruhe Institute of Technology (KIT), Campus North, Institute of Nuclear Physics, PO Box 3640, Karlsruhe, Germany*

[6]*Monash Centre for Astrophysics, School of Physics and Astronomy, Monash University, VIC 3800, Australia*

[7]*Research School of Astronomy and Astrophysics, The Australian National University, Canberra, ACT 2611, Australia*

[8]*School of Physics and Astronomy, University of Edinburgh, United Kingdom*

[9]*CERN, CH-1211 Geneva 23, Switzerland*

[10]*E.A. Milne Centre for Astrophysics, Dept. of Physics & Mathematics, University of Hull, United Kingdom*

[11]*Institute of Applied Physics, Goethe University Frankfurt, Frankfurt, Germany*

(Received 28 November 2016; revised manuscript received 11 May 2017; published 28 August 2017)

Accelerator mass spectrometry (AMS) represents a complementary approach for precise measurements of neutron capture cross sections, e.g., for nuclear astrophysics. This technique, completely independent of previous experimental methods, was applied for the measurement of the ^{54}Fe$(n,\gamma)^{55}$Fe reaction. Following a series of irradiations with neutrons from cold and thermal to keV energies, the produced long-lived ^{55}Fe nuclei ($t_{1/2} = 2.744 + -0.009$) yr) were analyzed at the Vienna Environmental Research Accelerator. A reproducibility of about 1% could be achieved for the detection of ^{55}Fe, yielding cross-section uncertainties of less than 3%. Thus, this method produces new and precise data that can serve as anchor points for time-of-flight experiments. We report significantly improved neutron capture cross sections at thermal energy ($\sigma_{\rm th} = 2.30 \pm 0.07$ b) as well as for a quasi-Maxwellian spectrum of $kT = 25$ keV ($\sigma = 30.3 \pm 1.2$ mb) and for $E_n = 481 \pm 53$ keV ($\sigma = 6.01 \pm 0.23$ mb). The new experimental cross sections have been used to deduce improved Maxwellian-averaged cross sections in the temperature regime of the common s-process scenarios. The astrophysical impact is discussed by using stellar models for low-mass asymptotic giant branch stars.

DOI: 10.1103/PhysRevC.96.025808

I. INTRODUCTION

Ultrasensitive single-atom counting via accelerator mass spectrometry (AMS) [1–3] offers opportunities for precise measurements of neutron capture cross sections. Direct atom counting of the reaction products provides a powerful complement of the conventional activation method because it is essentially independent of the half-life and decay characteristics of the reaction product, thus reducing the related uncertainties of the traditional activity technique [3–5]. As a new method, activation combined with subsequent AMS measurements gives results independent of existing previous experimental work. This technique was used here for a precise measurement of the ^{54}Fe$(n,\gamma)^{55}$Fe reaction.

Neutron capture cross sections at the relevant neutron energies between 1 and a few 100 keV are the essential nuclear physics input for the s-process nucleosynthesis.

The s process is composed of two major parts, a main component, which is responsible for the mass region from Y to Bi, and a weak component, which contributes to the region from Fe to Sr. In particular, the weak s process has been found to be very sensitive to the neutron capture cross sections of the isotopes near the seed distribution around Fe [6]. In the mass region of the weak s process, however, stellar neutron capture cross sections are often not available with the required accuracy of $\leqslant$2%–5% [7]. Experimental data suffer from large uncertainties and, even more important, discrepancies between different measurements are often much larger than the quoted uncertainties. As a consequence, insufficient knowledge of stellar cross-section data below $A = 120$ limits our understanding of the weak-s-process contribution to the solar system abundance distribution and to the galactic chemical evolution.

The information on keV-neutron capture cross sections has been summarized in compilations of Maxwellian-averaged cross sections (MACSs) for s-process applications [8–10]. In spite of the numerous data in the literature, these collections clearly exhibit the need for significant MACS improvements to

*anton.wallner@anu.edu.au

†Present address: TRIUMF, Vancouver BC, Canada.

‡NuGrid Collaboration, http://www.nugridstars.org

resolve discrepancies and/or to reach the necessary accuracy of 2%–5% [7] by dedicated precision measurements. Activation with AMS represents a truly complementary approach for precise measurements of neutron capture cross sections.

The present study of the ^{54}Fe$(n,\gamma)^{55}$Fe cross section is motivated by these aspects, i.e., to remove previous discrepancies but also to provide a sensitive test for the treatment of broad s-wave resonances in the analysis of time-of-flight (TOF) experiments. The proper strength of such resonances, which can dominate the MACS values in typical s-process environments, are difficult to extract from measured data. Because of their very large neutron widths, the scattering probability exceeds the capture channel by orders of magnitude, and the corrections for the effect of scattered neutrons are often obscuring the capture signal [11]. This inherent problem of TOF measurements, which has to be treated by extensive simulations of the particular experimental situation [12], is avoided in careful activation measurements.

Precise neutron capture cross sections are important quantities for reproducing the elemental abundance pattern. To fully exploit the potential of the s process as an abundance reference, it is necessary to establish an accurate set of the underlying nuclear physics data. In this context, neutron capture cross sections in the keV energy range are particularly important because of their strict correlation with the emerging s abundances and their effect on the overall neutron balance.

In the course of these investigations the s process plays a key role because the s abundances can be reliably quantified and in turn serve to derive the r abundances via the residual method [7]. This method is of particular interest because an increasing number of abundance observations in very rare, ultra-metal-poor stars in the galactic halo indicates abundance patterns that scale approximately with the solar r component for elements heavier than barium [13], but with star-to-star variations questioning the paradigm of a robust r-process production [14]. For lighter elements, there are significant discrepancies. Differences of the order of 20% are also found between the solar s-process abundances in the mass range $90 \leqslant A \leqslant 140$ and the results of galactic chemical evolution studies [15]. This result for the s process is mainly due to the achievements of nuclear astrophysics in the past decades [16].

Indications of neutron capture on ^{54}Fe have been found via isotopic ratios in different types of presolar SiC grains that condensed in supernovae ejecta and in the envelopes of low-mass asymptotic giant branch (AGB) stars and were trapped in pristine meteorites in the early solar system [17]. In these grains, Fe isotopic abundances are composed of normal pristine material and stellar matter processed by neutron capture. While the normal material carries the signature of galactic chemical evolution, the stellar material is determined by the respective (n,γ) cross sections, which are, therefore, crucial for quantitative analyses.

Meaningful analyses of the characteristic signatures preserved in presolar grains require also accurate cross sections with uncertainties of order of a few percent. The present status is far from being adequate, especially for the lighter elements.

Most of the ^{54}Fe in the universe is, however, made by explosive Si- and O-burning in core-collapse supernovae [18] and in thermonuclear supernovae [19]. ^{54}Fe is not produced in the s process in significant quantities but is instead depleted by neutron capture, according to its cross section. Small amounts of ^{54}Fe can be potentially produced by different types of p processes (see, e.g., Refs. [20,21]), but with negligible relevance for the galactic inventory. This suggests a precise knowledge of the ^{54}Fe(n,γ) cross section itself at keV energies will *a priori* not be crucial for the galactic chemical evolution and the s-process abundance distribution.

However, because large stellar physics uncertainties are still affecting theoretical predictions of the s process, a set of precise experimental nuclear reaction rates is a fundamental requirement to tackle these challenges. Further improvements in the standard prescriptions of s- and/or r-process nucleosynthesis are clearly needed for a refined view on the origin and enrichment of the elements in the Universe.

Given the existing discrepancies between evaluations and experimental data, and the above-mentioned difficulties in the TOF method, the AMS approach will help to study the possible existence of systematic uncertainties in previous measurements with an independent experimental approach. Another advantage of AMS as a complementary method is that it requires only small sample masses of the order of mg, thus scattering corrections inherent to TOF measurements are completely avoided. There are only a few cases where AMS can produce data precise at the level of 1%–2%; the measurement of ^{55}Fe belongs to this category. Thus, this reaction can serve as an anchor point for TOF results.

The paper is organized in the following way: Existing data in the literature are summarized in Sec. II. The following Secs. III and IV deal with the neutron activations and the AMS measurements. Data analysis and results are presented in Sec. V, the astrophysical aspects are discussed in Sec. VI, and a summary is given in Sec. VII.

II. PREVIOUS DATA

The present experiment is the first attempt to determine the ^{54}Fe(n,γ) cross section at keV energies via the activation method. This method had not been used so far because the very weak signals from the EC decay of ^{55}Fe are difficult to detect quantitatively. All previous data were, therefore, obtained by TOF measurements, starting with the work of Beer and Spencer [22], who reported capture and transmission data in the energy range 5 to 200 keV and 10 to 300 keV, respectively, but were missing the important s-wave resonance at 7.76 keV, which contributes about 30% to the MACS value at $kT = 30$ keV. Therefore, these results have been omitted in the further discussion.

The first complete list of the capture resonance parameter $k_\gamma = g\Gamma_n\Gamma_\gamma/\Gamma$ (capture kernel) in the astrophysically relevant energy from 0.1 to 500 keV was obtained by Allen *et al.* at the Oak Ridge Electron Linear Accelerator (ORELA, Oakridge, ORNL) [23,24]. Because this measurement was carried out with a rather thick sample of 2 at/barn, neutron multiple scattering and the detector response to scattered neutrons were causing significant background effects. For the broad s-wave resonances below 100 keV, which dominate the stellar cross section of ^{54}Fe, large corrections of up to 30% and 50% had to be considered for these effects, respectively.

TABLE I. Comparison of previous experimental results for the MACS of ^{54}Fe at $kT = 30$ keV with data from compilation and major data libraries.

Data from	$\langle\sigma v\rangle/v_T$ (mbarn)
n_TOF (expt) [26,27]	28.5±1.6
GELINA (expt) [25]	27.6 ± 1.8
ORNL (expt) [23,24]	33.6 ± 2.7
KADoNiS (comp) [9]	29.6 ± 1.3
ENDF-B/VII.1 (eval) [28]	21.6 ± 2.7
JENDL-4.0 (eval) [29]	21.6
JEFF-3.2 (eval) [30]	21.6

These corrections could be considerably reduced in a subsequent measurement by Brusegan *et al.* at the Geel Electron Linear Accelerator (GELINA, Joint Research Centre: Institute for Reference Materials and Measurements, Geel) [25]. With a much thinner sample of only 0.023 at/barn, the set of capture kernels could be significantly improved in the investigated neutron energy range below 200 keV.

Recently, Giubrone and the n_TOF collaboration [26,27] took advantage of the intense, high-resolution neutron source at CERN for further improving the capture data of ^{54}Fe from thermal to 500 keV. By reducing the sample dimensions again by factors of 3 and 25 in thickness and mass, respectively, and by application of refined analysis methods the set of resonance parameters could be obtained with unprecedented accuracy.

For a thermal energy of $kT = 30$ keV the MACS values deduced from these TOF measurements are compared in Table I with data from the KADoNiS v0.3 compilation (www.kadonis.org) as well as with the results calculated from the evaluated cross sections in the main data libraries ENDF/B-VII.1 [28], JENDL-4.0 [29], and JEFF-3.2 [30]. The KADoNiS value represents an average of the older TOF measurements [25] and [23,24]. In view of the consistent results of the refined measurements [25,26] it is surprising to find that the MACS values obtained with the evaluated cross sections are about 30% smaller. This situation clearly underlines the need for the present measurement, which is based on a completely independent experimental technique.

With respect to the thermal cross-section value, according to the compilation of Mughabghab [31], the thermal cross section of $\sigma_{\text{th}} = 2.25 \pm 0.18$ barn exhibits a comparably large uncertainty of 8% which again reflects the difficulty of quantifying the reaction product ^{55}Fe. We developed our measurement technique first with activations at cold and thermal neutron energies because they exhibit about 100 times higher neutron capture cross sections compared with keV energies.

III. NEUTRON IRRADIATIONS

A. Activations with thermal neutrons at Atominstitut, Vienna

The activations with thermal neutrons ($kT = 25$ meV; 300 K) were performed at the Training, Research, Isotope Production, General Atomic (TRIGA) Mark-II reactor at the Atominstitut in Vienna (ATI) in a well-characterized thermal spectrum. The neutron flux at the irradiation position about 1 m from the core was $\sim 3.7 \times 10^{11}$ cm^{-2} s^{-1}. This position provides a thermal-to-epithermal flux ratio of 76 (verified via the Zr standard method; for details see Ref. [32]).

TABLE II. Irradiations at thermal neutron energies.

Sample	Irradiation time (s)	Neutron flux (10^{11} cm^{-2} s^{-1})	Monitor: thermal cross section (mbarn)
ATI-FeM	600	3.53 ± 0.18	^{94}Zr(n,γ): 49.4 ± 1.7
ATI-Fe2	600	3.73 ± 0.20	
ATI-FeA2	120	3.83 ± 0.29	
ATI-FeA4	73	3.62 ± 0.19	

In total, four irradiations between 1 and 10 minutes were performed by using Zr foils as flux monitors (Table II). The Fe samples were prepared from metal powder of natural isotopic composition (5.845 ± 0.035% ^{54}Fe, 91.754 ± 0.036 ^{56}Fe) [33]. An amount of about 500 mg Fe powder, which was acquired from two different providers (Merck and Alfa Aesar), was encapsulated in plastic vials. The neutron fluence was determined by means of Zr foils attached to the vials via the induced ^{95}Zr activity, using the thermal cross-section value for ^{94}Zr(n,γ) of (0.0494 ± 0.0017) barn [31]. The activities of these foils indicated flux variations of up to 5% between different activations reflecting small variations in the reactor power between these activations.

B. Activations with cold neutrons at Budapest Neutron Centre

The irradiations were conducted at the 10 MW research reactor of the Budapest Neutron Centre (BNC) using the facilities for prompt gamma activation analysis (PGAA) and the neutron-induced prompt gamma-ray spectrometer (NIPS) [34–36]. The neutrons from the reactor core were transported in a neutron guide tube, resulting in a cold neutron beam with an average neutron energy of 10 meV. The typical neutron flux at the irradiation position was 3 and 4×10^7 cm^{-2} s^{-1} (thermal equivalent) for the NIPS and PGAA station, respectively.

Two iron samples 6 mm in diameter were prepared: one consisting of 44 mg metal powder of natural isotopic composition and the second of almost pure ^{54}Fe (45.2 mg, 99.85% enrichment, STB Isotope GmbH). Approximately 20 mg of Au powder were homogeneously mixed with the iron powder and the mixture was pressed into pellets. The pellets were then sandwiched by two Au foils of the same diameter, forming a stack Au-(Fe/Au)-Au. This geometry was identical to the irradiation setup used for the measurement of the ^{235}U$(n,\gamma)^{236}$U and the ^{238}U$(n,\gamma)^{239}$U reaction at this neutron energy [5].

The Au foils and the Au powder in the iron matrix were used to deduce the thermal equivalent neutron fluence in the irradiations, which lasted for about 1 and 4 d, respectively (Table III) [37]. The fluence was determined from the induced ^{198}Au activity of the monitor foils by using the thermal cross-section value for ^{197}Au(n,γ) of 98.66 ± 0.14 barn [38–40].

TABLE III. Irradiations at cold neutron energies.

Sample	Irradiation time (min)	Neutron flux (10^7 cm^{-2} s^{-1})	Monitor: thermal cross section (barn)
BNC-FeM	5449	3.19 ± 0.07	^{197}Au(n,γ): 98.66 ± 0.14
BNC-Fe4	1481	4.46 ± 0.10	

C. Activations with keV neutrons

The irradiations with keV neutrons were carried out at the Karlsruhe Institute of Technology (KIT) using the 3.7 MV Van de Graaff accelerator. Neutrons were produced via the ^{7}Li$(p,n)^7$Be reaction by bombarding 5- and 30-μm thick layers of metallic Li on a 1-mm-thick water-cooled Cu backing with proton beam currents of 80-90 μA. The thickness of the Li layers was controlled by means of a calibrated oscillating quartz monitor. During the irradiations, the neutron flux history was registered in intervals of 90 s by a ^{6}Li-glass detector positioned 1 m from the neutron target. With this information it is possible to properly correct the fraction of decays during irradiations, including the fact that the Li targets degrade during the activation. A schematic sketch of the experimental setup is shown in Fig. 1.

Two sets of Fe samples from two different providers (see Sec. III A) were prepared by pressing high-purity metal powder of natural isotopic composition into thin pellets 6 mm in diameter. During the activations the Fe samples were sandwiched between thin gold foils of the same diameter. The sample properties are summarized in Table IV.

For probing the neutron energy ranges of relevance in AGB stars and in massive stars, proton energies of 1912 and 2284 keV were chosen, respectively. With a proton energy of 1912 keV, 31 keV above the threshold of the ^{7}Li(p,n) reaction and using Li layers 30 μm in thickness, kinematically collimated neutrons are produced, which are emitted into a forward cone of 120° opening angle. Integration over this neutron field yields a quasistellar Maxwell–Boltzmann

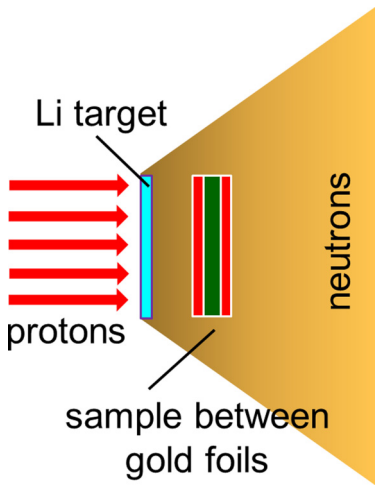

FIG. 1. Schematic sketch of the setup used for the neutron activations at the Karlsruhe Van de Graaff.

TABLE IV. Sample characteristics and parameters of activations at keV neutron energies.

Sample[a]	Thickness (mm)	Mass (mg)	Activation time (h)	Average n flux[b] (10^9 s^{-1} cm^{-2})
KIT-1M	1.8	334.8	251.5	0.84
KIT-2A	2.3	369.5	369.5	0.95
Gold foils	0.03	16.1–16.8		
KIT-3M	1.4	258.5	54.5	6.99
KIT-4A	1.2	188.4	44.3	5.37
Gold foils	0.02	11.3–11.8		

[a]Fe samples pressed from metal powder, gold foils cut from metal sheets; all samples 6 mm in diameter.
[b]Averaged over activation time.

(q-MB) spectrum for a thermal energy of $kT = 25 \pm 0.5$ keV [41].

Two activations have been carried out for each of the neutron energies. The main parameters of the irradiations are summarized in Table V. At the lower energy around 25 keV the sample sandwich was in direct contact with the target backing, because the maximal emission angle of 120° ensured that it was fully exposed to the quasistellar field (see, e.g., Refs. [42,43]) independent of the sample thickness. At $E_p = 2284$ keV, however, where neutron emission is nearly isotropic, a distance of 4 mm was chosen between Li target and sample for restricting the energy range of the neutron flux hitting the sample. At this higher proton energy 5-μm-thick Li layers have been used. The resulting neutron spectrum centered at 481 ± 53 keV full width at half maximum (FWHM) was calculated with the interactive Monte Carlo code PINO [44] with the actual irradiation parameters as input. The corresponding neutron spectra are plotted in Fig. 2.

For the gold reference cross section in the energy range of the 25 keV q-MB spectrum, the prescription of the new version KADoNiS v1.0 [45] has been followed by adopting the weighted average of recent data from measurements at GELINA [46] and n_TOF [47,48]. This choice is also in perfect agreement with a recent activation measurement [49] and the standards evaluation [39,40,50]. Note that the effective values for the 25 keV q-MB spectrum listed in column three of Table V are reflecting a change of 5.3% in the gold reference cross

TABLE V. Parameters for the irradiations at keV neutron energies.

Sample	E_p (keV)	Gold cross section[a] (mbarn)	Neutron fluence (10^{15} cm^{-2})
		q-MB[b] at $kT = 25$ keV	
KIT-1M	1912	632 ± 9	0.756 ± 0.023
KIT-2A	1912	632 ± 9	1.270 ± 0.038
		$\overline{E}_n = 481 \pm 53$ keV	
KIT-3M	2284	139.0 ± 1.4	1.370 ± 0.041
KIT-4A	2284	139.0 ± 1.4	0.857 ± 0.026

[a]Spectrum-averaged values.
[b]Quasi-Maxwell–Boltzmann distribution simulating a thermal spectrum at $kT = 25$ keV.

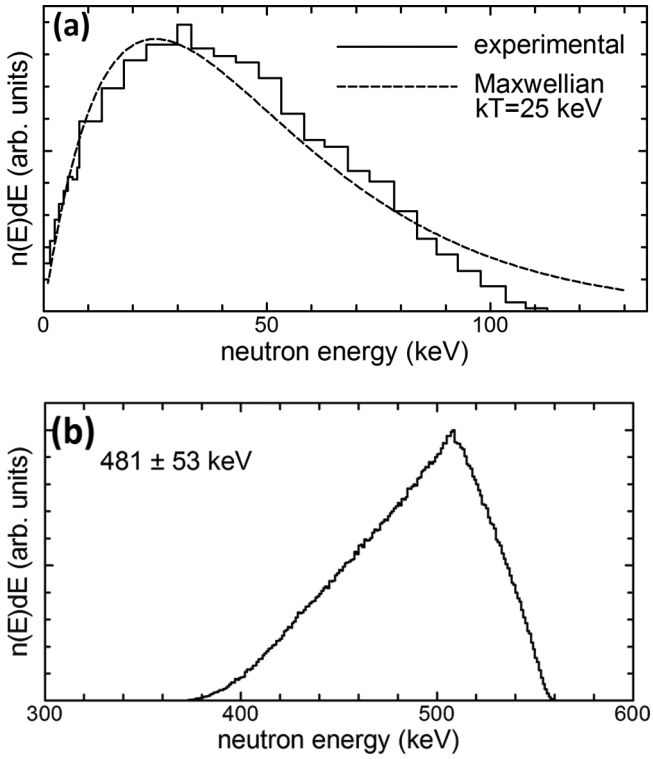

FIG. 2. Neutron energy distributions in the irradiations at the Karlsruhe Van de Graaff accelerator obtained with protons of (a) 1912 keV energy and (b) 2284 keV.

section compared with the values previously used in similar activation experiments.

For the 481 ± 53 keV spectrum, where the (n,γ) cross section of gold is an established standard [40,50], the evaluated data from the standards evaluation (and adopted by the ENDF/B-VII.1 library) have been used. The respective spectrum-averaged gold cross sections are listed in Table V.

D. Neutron fluence

The induced activities of the Au (activations at KIT and BNC) and Zr (activation at ATI) monitor foils were measured by using high-purity germanium (HPGe) detectors. The γ efficiency was calibrated with a set of accurate reference sources and was known with an uncertainty of $\pm 2.0\%$. The corrections due to coincidence summing and sample extension were minimized by keeping the distance between sample and detector much larger than the respective diameters.

The number of counts C in the characteristic 411.8 keV line in the Au γ-ray spectrum recorded during the measuring time t_m is related to the number of produced ^{198}Au, N_{198} at the end of irradiation by

$$N_{198} = \frac{C}{K_\gamma \epsilon_\gamma I_\gamma (1 - e^{-\lambda t_m}) e^{-\lambda t_w}}, \tag{1}$$

where ϵ_γ denotes the detector efficiency and t_w is the waiting time between irradiation and activity measurement. The decay rate $\lambda = 0.257\,28(2)$ d^{-1} and the intensity per decay, $I_\gamma = 95.62(6)\%$ of ^{198}Au were adopted from Ref. [51]. The factor K_γ describes the γ-ray self-absorption in the sample, which, for the thin gold samples used in this work, is to a very good approximation [52]

$$K_\gamma = \frac{1 - e^{-\mu x}}{\mu x}. \tag{2}$$

The γ-ray absorption coefficient μ was taken from Ref. [53]. The gold samples were $x = 20$–30 μm in thickness, yielding self-absorption corrections $K_\gamma = 0.996$–0.994. Accordingly, the associated uncertainties had no effect on the overall uncertainty budget and were neglected.

Similarly, the number of produced ^{95}Zr nuclei in the ATI irradiations was deduced from the decay rate $\lambda = 0.0108(1)$ d^{-1} and the intensity per decay, $I_\gamma = 44.27(22)\%$ for 724.2 keV and $I_\gamma = 54.38(22)\%$ for 756.7 keV (adopted from Ref. [54]).

The number of produced nuclei, N_{198} or N_{95} ($N_{\rm prod}$), can also be expressed by the neutron fluence $\Phi_{\rm tot} = \int_0^{t_a} \Phi(t)dt$, the corresponding spectrum-averaged capture cross section $\langle\sigma\rangle$, the decay correction f_b, and the number of irradiated atoms in the sample N as

$$N_{\rm prod} = \Phi_{\rm tot} N \langle\sigma\rangle f_b. \tag{3}$$

The factor f_b, which corrects for the fraction of activated nuclei that already decay during irradiation, is

$$f_b = \frac{\int_0^{t_a} \Phi(t) e^{-\lambda(t_a - t)} dt}{\int_0^{t_a} \Phi(t) dt}, \tag{4}$$

where $\Phi(t)$ denotes the neutron intensity during the irradiation and λ is the decay rate of the product nucleus ^{198}Au or ^{95}Zr.

In the short activations at ATI this correction is almost negligible because the half-life of the activation product ^{95}Zr was much longer than the irradiation times t_a. In the longer irradiations at BNC and KIT it had to be considered for the gold activities, where the half-life of $t_{1/2} = 2.6941(2)$ d is comparable to the irradiation times of about 1 and 4 d. Due to the constant neutron flux provided by the reactor, f_b can be determined by integrating Eq. (4).

In the ATI activations, the total production of ^{95}Zr consists of the thermal part ($\sigma_{\rm th} = 49.4 \pm 1.7$ mbarn) and the epithermal part (the resonance integral RI $= 280 \pm 10$ mbarn) [31,38] with the epithermal flux being 1/76 of the thermal flux for this irradiation setup [32]. Therefore, an additional 7% of the total ^{95}Zr production was due to the epithermal neutrons. This contribution was corrected for in the calculation of the thermal neutron fluence (Tables II and VIII).

For ^{54}Fe$(n,\gamma)^{55}$Fe, the ratio of epithermal to thermal cross section is much lower, with $\sigma_{\rm th} = 2.25 \pm 0.18$ barn and RI $= 1.2 \pm 0.1$ barn [31,38], about one tenth of the ^{94}Zr case. The equivalent correction for the ATI activation for ^{54}Fe$(n,\gamma)^{55}$Fe was $<1\%$. The final accuracy of the neutron fluence for the ATI setup was dominated by the uncertainty of the ^{94}Zr$(n,\gamma)^{95}$Zr cross section (3.4%), the epithermal correction and reproducibility of the irradiation geometry (3%), and the γ efficiency of the Ge detector (2%). In the end the fluence for the ATI samples could be determined with an uncertainty of about 5.6% (see Table VI).

For the cold neutron beam at the BNC the neutron spectrum is characterized by a pure 1/v shape with energies below

TABLE VI. Uncertainty contributions for the thermal cross-section value.

Source of uncertainty	Uncertainty (%)
Neutron fluence	ATI / BNC[a]
Zr / gold cross section	3.4/0.1
Epithermal correction	3 / 0[a]
Mass of Zr / gold samples	<0.2 / <0.1
γ efficiency	2.0
γ intensity per decay	0.5/0.12
Time factors	<0.1
Total fluence:	5.6 / 2.0%
AMS measurement	
PTB standard	1.5
Atom counting	<1
^{56}Fe current	0.6
AMS reproducibility	1.5
Total AMS:	2.5%
Total: ATI (thermal) / BNC (cold)	6.4 / 3.2

[a]For thermal and cold neutrons, respectively.

50 meV [36]. Because the cross sections of ^{197}Au and ^{54}Fe also exhibit a 1/v shape in this energy range, the reaction rates are scaling in exactly the same way from cold to thermal energies. Accordingly, there are no corrections for epithermal neutrons in this case. In addition, these irradiations were performed in a well-defined geometry with the sample stack mounted perpendicular to the neutron beam. By comparison of the activities of the gold powder mixed with Fe in the pellets with the front and back foils in the stack it could be demonstrated that the respective fluence values were consistent within 1%, thus constraining possible corrections for inhomogeneities of the beam and scattering effects. The effective fluence could be derived with an accuracy of 2% as detailed in Table VI.

IV. ACCELERATOR MASS SPECTROMETRY MEASUREMENTS

Because ^{55}Fe decays almost completely into the ground state of ^{55}Mn [$t_{1/2} = 2.744(9)$ yr, with only 1.3×10^{-7} γ rays per decay], the ^{55}Fe nuclei were directly counted—prior to their decay to stable ^{55}Mn—by AMS measurements at the Vienna Environmental Research Accelerator (VERA), a state-of-the-art AMS facility based on a 3 MV tandem [5,55]. A schematic view of the VERA facility is shown in Fig. 3, including the detection devices for recording the stable ^{54,56}Fe and the low-intensity ^{55}Fe ions.

Negatively charged Fe ions from a cesium sputter source are pre-accelerated and mass analyzed in a low-energy spectrometer. In the extracted beam, isobaric background due to ^{55}Mn was completely suppressed because ^{55}Mn does not form stable negative ions [56]. For Fe ions the terminal voltage of the tandem accelerator was set to 3 MV. Remaining molecular beam impurities are completely destroyed in the terminal stripper, thus eliminating any isobaric interferences with the subsequent mass-selective filters (see Fig. 3). After acceleration ions with charge 3^+ and an energy of 12 MeV were selected in the analyzing magnet. The stable ^{54,56}Fe ions were counted as particle currents with Faraday cups, whereas the low-intensity ^{55}Fe fraction in the beam was subjected to further background suppression by the electrostatic analyzer and was eventually recorded with one of the energy-sensitive detectors.

The isotopes ^{56}Fe, ^{54}Fe, and ^{55}Fe were sequentially injected as negative ions into the accelerator. By rapidly varying the respective particle energies of the different isotope, the different masses of the Fe isotopes were accommodated, resulting in the same mass-energy product. In this way the particles were adjusted to the same magnetic rigidity at the injection magnet (so-called beam sequencer, not shown in Fig. 3) and consequently they followed sequentially the same beam trajectories. The stable Fe isotopes were analyzed by current measurements with Faraday cups after the injection magnet and after the analyzing magnet (for ^{56}Fe and ^{54}Fe, respectively). The beam intensity of ^{55}Fe was measured as count rate with one of the particle detectors. This sequence was repeated five times per second with millisecond injection times for ^{54,56}Fe, whereas the remaining 95% of the time were used for ^{55}Fe counting. The transmission through the accelerator was monitored by the currents measured at the low- and the high-energy side. Because the measured ^{54}Fe and ^{56}Fe currents are defined by the isotopic composition of natural iron, the AMS runs of standards and irradiated samples could be based on both the ^{54}Fe and the ^{56}Fe beam.

The ratio of the ^{55}Fe/^{56}Fe beam intensities produced in the irradiations was of the order of 10^{-11} to 10^{-12}. The ^{55}Fe/^{56}Fe ratios from a sputter sample, prepared from one of the samples irradiated at ATI, are plotted in Fig. 4(a). These data were measured during one specific AMS beam time. The solid and dashed lines represent the weighted mean and the standard deviation of the mean for the respective samples.

Figures 4(b) and 4(c) represent data for two blank samples assumed to be free of ^{55}Fe. The ^{55}Fe/^{56}Fe ratio was measured at VERA with a background of typically $<2 \times 10^{-15}$ [Fig. 4(c)] in the detector positions 2 and 3 (see Fig. 3). Detector position 1, located after the electrostatic analyzer, but before an additional magnetic filter, gave a ^{55}Fe/^{56}Fe background of $2–3 \times 10^{-14}$. This higher background originated from a few ^{54}Fe ions that were still accepted at this detector position. However, these ions were suppressed by more than a factor of 20 at the other detector positions further downstream. Accordingly, the background contributed only less than 0.3 counts per hour to the observed ^{55}Fe count rate of about one every few seconds.

Several AMS beam times were combined to give the final isotope ratio. Under these conditions, counting statistics contributed to <1% to the final AMS uncertainty and a reproducibility of 1.5% could be reached (see Table VI) [3,57,58].

The ^{55}Fe/^{56}Fe ratios from the irradiations at KIT, as measured during the various AMS beam times, are plotted in Fig. 5. Figure 5(a) gives the data for the two samples activated in the quasistellar Maxwell–Boltzmann spectrum, Fig. 5(b) represents the data for the two samples activated at the higher energies around 481 keV. The solid and dashed lines represent the weighted mean and the standard deviation, respectively, of the mean for the respective samples. All data are corrected

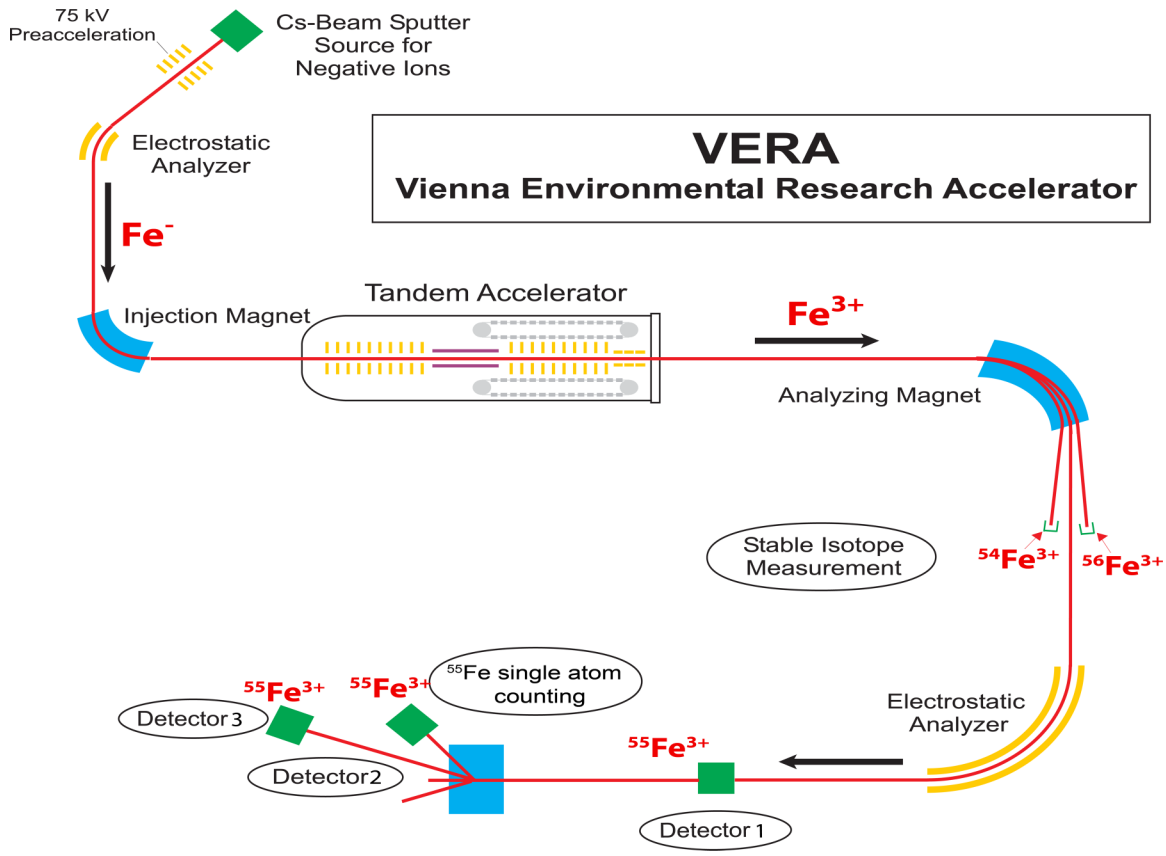

FIG. 3. Schematic layout of the AMS facility VERA. Negative Fe ions were extracted from the ion source and mass analyzed before the tandem accelerator. After stripping in the terminal the three-fold positively charged (3^+) ions with an energy of 12 MeV were selected for analysis. The stable ^{54,56}Fe nuclei were measured with Faraday cups, and the rare nuclide ^{55}Fe was counted in one of the three subsequent particle detectors (see text for details).

for decay of ^{55}Fe since their production in the various activations.

Because inherent effects such as mass fractionation, machine instabilities, or potential beam losses between the current measurement and the respective particle detector are difficult to quantify in an absolute way to better than 5% to 10%, accurate AMS measurements depend on well-defined reference materials. Therefore, the isotope ratios ^{55}Fe/^{54,56}Fe have been measured relative to an ^{55}Fe/^{54,56}Fe standard produced by means of a ^{55}Fe reference solution by the German metrology laboratory at PTB Braunschweig, with a certified 1σ uncertainty of $\pm 1.5\%$ [37,58]. Details on the AMS procedure for ^{55}Fe measurements are given in Refs. [3,57,58].

V. DATA ANALYSIS AND RESULTS

The spectrum-averaged ^{54}Fe(n,γ) cross section can be directly calculated from the total neutron fluence Φ_{tot}, and the isotope ratio ^{55}Fe/^{56}Fe and ^{55}Fe/^{54}Fe measured via AMS,

$$\langle\sigma\rangle = \frac{1}{\Phi_{\text{tot}}}\frac{^{55}\text{Fe}}{^{54}\text{Fe}} = \frac{1}{\Phi_{\text{tot}}}\frac{^{55}\text{Fe}}{^{56}\text{Fe}}\frac{^{56}\text{Fe}}{^{54}\text{Fe}}, \tag{5}$$

where $^{56}\text{Fe}/^{54}\text{Fe} = N_{56}/N_{54} = 15.70 \pm 0.09$ corresponds to the natural isotope ratio in the sample (91.75% and 5.85%, respectively) [33]. Note the particular advantage of the AMS method, i.e., that the cross section is determined completely independent of the sample mass and the decay properties of the product nucleus.

The main contributions to the total 3% uncertainty of the neutron fluence at KIT and BNC are due to the γ efficiency of the HPGe detector and to the Au reference cross sections (Tables VI and VII). For ATI, in addition, the ^{94}Zr$(n,\gamma)^{95}$Zr cross section (3.4%) and the epithermal correction (3%) have to be taken into account. The measured ^{55}Fe/^{56}Fe ratios are listed in Tables VIII and IX together with the resulting cross sections. The uncertainties associated with the AMS measurement are determined by the ^{55}Fe standard (1.5%), the ^{56}Fe current (0.6%), the reproducibility of the AMS runs (1.5%), and the counting of the unstable ^{55}Fe nuclei (3%–6% for individual AMS runs). The statistical uncertainties become $<2\%$ when all AMS beam times are combined. The quadratic sum of these contributions yields an effective AMS uncertainty of 3% (Tables VI and VII).

A. Thermal cross section

The measured cross sections are listed in Table VIII. Both thermal cross-section values deduced from the BNC and ATI activations [37] show a very good agreement (see Fig. 6). The scatter of the individual results is small ($\pm 2\%$) and the

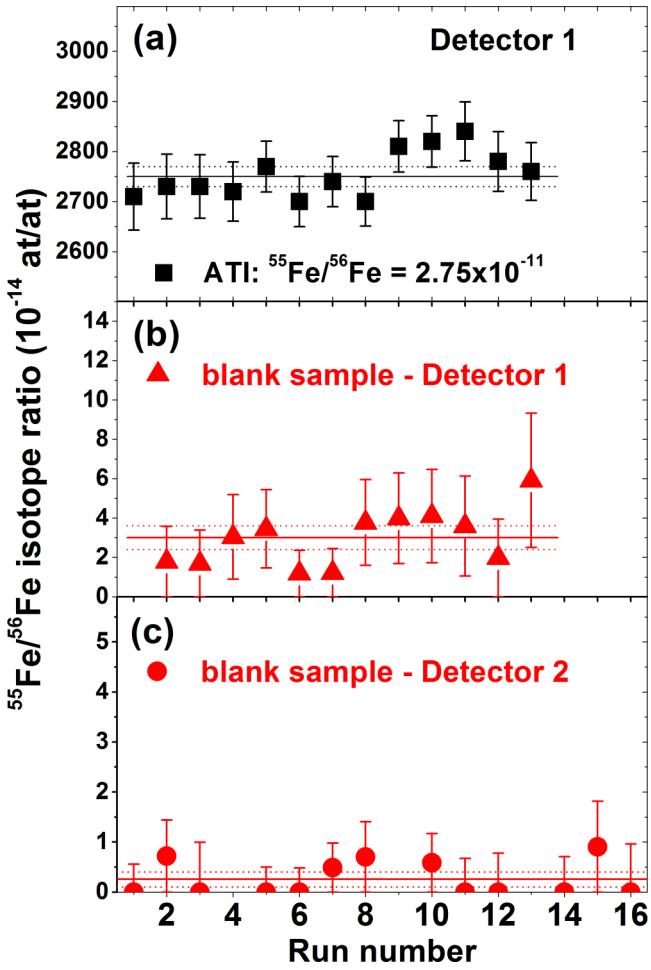

FIG. 4. Individual ^{55}Fe/^{56}Fe ratios as obtained during one AMS beam time. The upper panel (a) gives the data for a test sample irradiated at ATI with thermal neutrons. The two lower panels (b) and (c) represent the data for two unirradiated blank samples assumed to have negligible ^{55}Fe content. Measurements in panel (c) show a reduced measurement background (average ^{55}Fe/^{56}Fe ratio $<10^{-15}$ at detector position 2). The solid and dashed lines represent the weighted mean and the standard deviation of the mean, respectively, for the respective samples.

TABLE VII. Uncertainty contribution for the spectrum-averaged cross sections at keV energies.

Source of uncertainty	Uncertainty (%)
Neutron fluence	
Gold cross section	1.5/1.0[a]
Mass of gold samples	0.3
γ efficiency	2.0
γ intensity per decay	0.12
Time factors	<0.1
AMS measurement	
PTB standard	1.5
Atom counting	<2
^{56}Fe current	0.6
AMS reproducibility	1.5
Total	4.0/3.8

[a]For neutron energies of 25 (q-MB) and 481 keV, respectively.

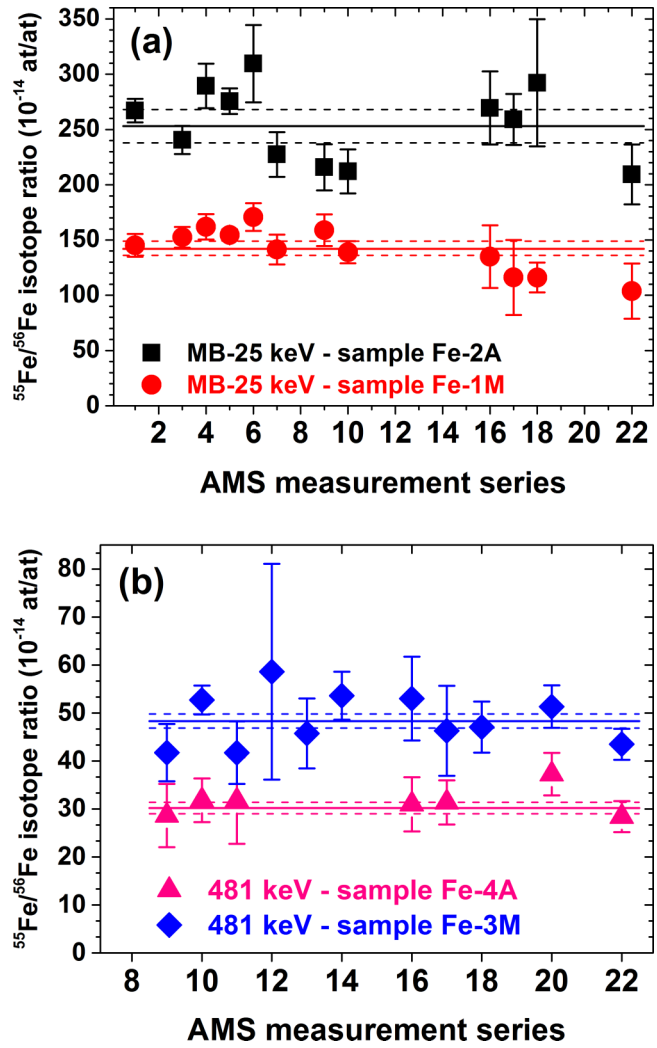

FIG. 5. Mean ^{55}Fe/^{56}Fe ratios as obtained during the various AMS beam times. The upper panel (a) gives the data for the two samples irradiated at KIT with a quasistellar Maxwell–Boltzmann spectrum, the lower panel (b) represents the data for the two samples irradiated at KIT with higher energies around 481 keV. The solid and dashed lines represent the weighted mean and the standard deviation of the mean for the respective samples.

TABLE VIII. Results from the activations at cold and thermal neutron energies.

Sample	Neutron fluence[a] (10^{13} cm^{-2})	^{55}Fe/^{54}Fe (10^{-10} at/at)	Thermal cross section (barn)
ATI-FeM	21.2 ± 1.1	4.69 ± 0.10	2.21 ± 0.15
ATI-Fe2	22.4 ± 1.2	5.10 ± 0.13	2.28 ± 0.15
ATI-FeA2	4.59 ± 0.35	1.03 ± 0.022	2.24 ± 0.15
ATI-FeA4	2.65 ± 0.14	0.61 ± 0.02	2.30 ± 0.15
Mean			2.26 ± 0.15
BNC-FeM	1.042 ± 0.025	0.246 ± 0.008	2.36 ± 0.07
BNC-Fe4	0.396 ± 0.009	0.091 ± 0.002	2.29 ± 0.06
Mean			2.31 ± 0.07
Weighted mean			2.30 ± 0.07

[a]Thermal equivalent neutron fluence (ATI values include 7% correction for epithermal contribution of Zr monitor foils).

TABLE IX. Results for the activations at keV neutron energies.

Energy (keV)	Sample	^{55}Fe/^{56}Fe (10^{-12})	$\langle\sigma\rangle$[a] (mbarn)	ENDF/B[a] -VII.1
25 (qMB)	KIT-1M	1.42 ± 0.05	31.3 ± 1.5	
	KIT-2A	2.53 ± 0.11	29.6 ± 1.4	
	Adopted		30.3 ± 1.2	22.6
481±53	KIT-3M	0.48 ± 0.01	6.01 ± 0.28	
	KIT-4A	0.30 ± 0.01	6.02 ± 0.23	
	Adopted		6.0 ± 0.2	7.3

[a]Spectrum-averaged cross sections.

final uncertainty is dominated by systematic contributions. The weighted mean gives our thermal cross-section value of 2.30 ± 0.07 barn, which is well compatible with the value of 2.25 ± 0.18 barn recommended in Ref. [31], but a factor of 2.5 more accurate (see Table VIII). Our data also fit well to the recently published value of Belgya *et al.*, which is based on an improved knowledge of the decay scheme of ^{55}Fe, resulting in a thermal cross section of 2.29 ± 0.05 barn [59].

B. Spectrum-averaged cross sections at keV energies

For the Karlsruhe activations at keV energies the effective gold reference cross section had to be determined by folding with the experimental neutron energy distributions, i.e., the quasi-MB spectrum at $kT = 25$ keV and the spectrum around 481 ± 53 keV. The cross section of the ^{197}Au(n,γ) reaction was adopted according to the recommendation in the new version KADoNiS v1.0 [45] and yields spectrum-averaged Au cross sections of ^{197}Au with uncertainties of 1.5% and 1% (Table V).

The keV-neutron flux produced at the Karlsruhe Van de Graaff showed considerable nonuniformities due to the decreasing performance of the Li targets as well as to fluctuations in the beam intensity. Therefore, the correction factor f_b had to be evaluated by numerical integration of Eq. (3) by using the time dependence of the neutron flux that was recorded by the ^{6}Li-glass detector as mentioned above.

The comparison in Table IX shows that the present results are 34% higher at 25 keV and 20% lower at 481 keV than obtained by folding the evaluated cross section from the ENDF/B-VII.1 library with the respective neutron spectra. While the evaluated data imply a rather weak energy dependence, the present results are consistent with a $1/\sqrt{E_n}$ dependence on energy, in full agreement with the cross-section shape implied by the experimental TOF data [23–27]. Therefore, this energy trend is to be preferred for improving the MACS values (see Sec. VI A).

For comparison with the present result, the TOF data were averaged over the 25 keV-qMB distribution $N(E)$ by using the approximation [62]

$$\langle\sigma\rangle = \frac{\int \sigma_{\rm th}\sqrt{\frac{25\times10^{-6}}{E}}N(E)dE + \sum_i N(E)_i A_{\gamma,i}}{\int N(E)dE}, \quad (6)$$

where the first term in the numerator represents the $1/\sqrt{E_n}$ extrapolation of our new thermal cross-section value $\sigma_{\rm th} =$

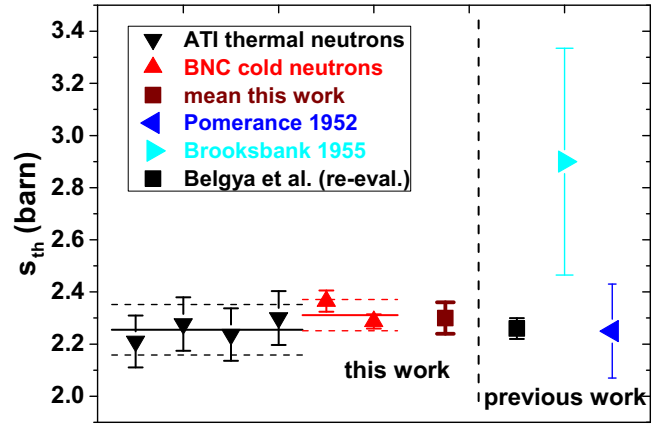

FIG. 6. Comparison of the thermal cross-section values obtained in this work from two independent activations with thermal (ATI) and cold (BNC) neutrons. Also plotted are the two previous experiments from more than 60 years ago by Brooksbank *et al.* [60] and by Pomerance [61]. The weighted average (square) of our work is in very good agreement with the value of Ref. [61], which was the basis for the recommend value in Ref. [31]. Also plotted is a new value quoted by Belgya *et al.* that is based on an improved decay scheme of ^{55}Fe [59].

2.30 ± 0.07 mbarn (see Sec. V A). The resonance contribution is obtained by the sum of the resonance areas

$$A_{\gamma,i} = \frac{2\pi^2}{k_n^2}\frac{g\Gamma_\gamma\Gamma_n}{\Gamma_\gamma+\Gamma_n},$$

which are determined by the radiative and neutron widths Γ_γ, Γ_n, the wave number $k_n = (2.1968 \times 10^9)A/(A+1)\sqrt{E_n}$, and the statistical factor $g = (2J+1)/(2I+1)(2s+1)$. With this approximate prescription, the resonance parameters of Giubrone [26], Brusegan *et al.* [25], and Allen *et al.* [23,24] yield spectrum-averaged cross sections of 30.9, 30.5, and 32.8 mbarn, respectively. The weighted average of 31.3 ± 2.1 mbarn is about 3% higher than our value of 30.3 ± 1.2 mbarn, well within uncertainties.

An additional test was made by using the resonance parameters of Giubrone [26]. The contributions of the broad s-wave resonances have been expressed by a sum of Breit–Wigner terms,

$$\sigma(E_n) = \frac{\pi}{k_n^2}\frac{g\Gamma_\gamma\Gamma_n}{(E_n-E_{\rm res})^2+(\Gamma_\gamma+\Gamma_n)^2/4},$$

yielding a partial spectrum average of 9.6 mbarn. As the low-energy tails of these resonances contribute already a fraction of 834 mbarn to the thermal cross section, the $1/v$ extrapolation from thermal to 25 keV is reduced from 2.08 to 1.24 mbarn. The narrow resonances with $\ell > 0$ can again be treated as a weighted sum of the resonance areas and are found to contribute another 19.3 mbarn. In total, the Breit–Wigner approach gives 30.1 mbarn, in fair agreement with the 30.9 mbarn obtained via Eq. (6), thus justifying the use of this expression [63].

At this point it is interesting to note that the refined experiments [25,26] yield spectrum-averaged cross sections in significantly better agreement with the present result than

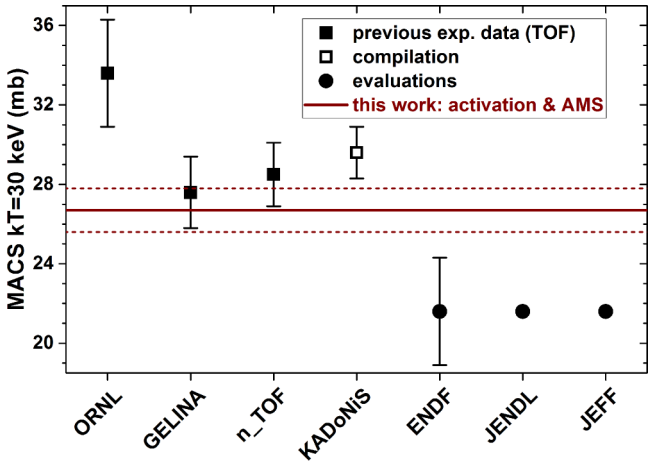

FIG. 7. Comparison of the present MACS value at $kT = 30$ keV with the recommended value in the compilation of Ref. [10], data obtained in previous TOF measurements [24–27] and calculated from the evaluated cross sections in the ENDF/B-VII.1 [28], JENDL-4.0 [29], and JEFF-3.2 [30] libraries.

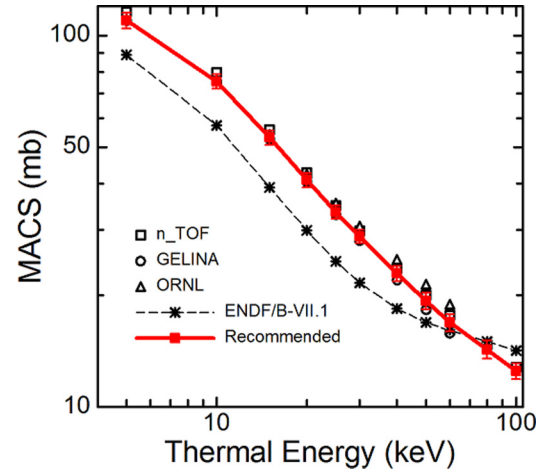

FIG. 8. Recommended MACS values between $kT = 5$ and 100 keV compared with data obtained with evaluated cross sections from ENDF/B-VII.1 [28] and from TOF-based experimental data [23,25,26] (see text for details).

the first attempt described in Refs. [23,24]. In fact, within uncertainties these values are consistent, indicating the proper treatment of neutron backgrounds in the analysis of the broad s-wave resonances, especially those at 7.8, 52.8, and 99.1 keV neutron energy (see Fig. 7).

VI. ASTROPHYSICAL ASPECTS

A. Maxwellian-averaged cross sections

In view of the difficulties with the energy dependence of the evaluated cross section, additional MACS values have been calculated from the experimental resonance data of Refs. [23,25,26] by using the approximation of Macklin and Gibbons [62],

$$\frac{\langle \sigma v \rangle}{v_T} = \sigma_{\rm th}\sqrt{\frac{25\times 10^{-6}}{kT}} + \frac{2}{\sqrt{\pi}}\frac{1}{(kT)^2}\sum_i A_{\gamma,i}E_i \exp\left(\frac{-E_i}{kT}|!\right),$$

where E_i denotes the resonance energy and kT is the thermal energy. As the sum in this equation ends at the maximum resonance energy of a given data set, the thermal spectrum is truncated at this energy. To keep the error caused by the truncation close to the experimental uncertainties, MACS values derived from the data in Refs. [23,25] have been limited to thermal energies below $kT = 60$ keV.

The comparison of the present MACS for $kT = 30$ keV in Fig. 7 shows good agreement with the refined TOF measurements performed at Geel [25] and at CERN/n_TOF [26,27], whereas the evaluated cross sections in the ENDF/B-VII.1 [28], JENDL-4.0 [29], and JEFF-3.2 [30] libraries are yielding incompatibly small values. The MACS in the KADoNiS [10] compilation is obviously biased by the high value from Refs. [23,24].

The temperature dependence of these results (Fig. 8) shows that the TOF data are providing a consistent trend, in accordance with the present results. In contrast, the trend obtained with the evaluated cross sections is clearly overestimating the MACS values above about 60 keV. Therefore, the temperature trend defined by the experimental TOF data sets has been adopted for the recommended MACS values in Table X.

These recommended MACS values are based on the adopted temperature trend, but are normalized to the measured spectrum-averaged cross section at 25 keV by a factor

$$NF = (30.3 \pm 1.2\ \text{mbarn})/31.5\ \text{mbarn} = 0.968 \pm 0.040,$$

where the denominator represents the corresponding mean value derived from the TOF measurements as described above. The uncertainties are composed of contributions from the measured spectrum-averaged cross section (±4.0%) and from the energy trend, which was estimated via the differences among the TOF-based MACS data (0% to 4.5%).

Figure 9 shows the MACS ratios of the ENDF/B-VII.1 [28] and KADoNiS v0.3 compilation [9,10] to the present

TABLE X. Recommended MACS values from this work (in mbarn) compared with data obtained with evaluated cross sections from ENDF/B-VII.1 [28] and from the KADoNiS v0.3 compilation [9,10].

kT (keV)	ENDF/B-VII.1	KADoNiS	This work
5	88.8	119	102 ± 5
10	57.3	81	69.9 ± 3.1
15	39.1	56	49.3 ± 2.2
20	29.9	43	37.9 ± 1.7
25	24.7	35	31.1 ± 1.3
30	21.6 ± 2.7	29.6 ± 1.3	26.7 ± 1.1
40	18.4	23.9	21.2 ± 1.0
50	16.9	20.9	17.9 ± 0.9
60	16.1	19.2	15.7 ± 0.8
80	15.0	17.4	13.3 ± 0.7
100	14.2	16.4	11.6 ± 0.6

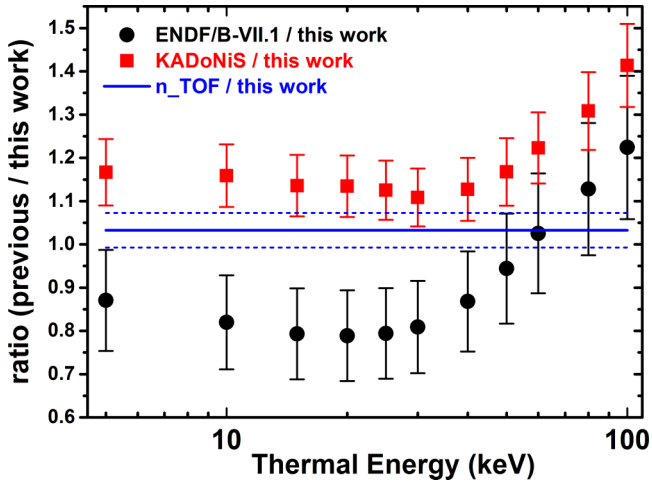

FIG. 9. Ratio of the MACS values obtained in previous work to this work using the temperature dependence found at CERN n_TOF [26,27]. Both, ENDF/B-VII.1 [28] and the KADoNiS v0.3 compilation [9,10] show a different energy dependence.

MACS values. The absolute scale is given by the present AMS measurement and the energy trend is based on the experimental TOF data given in Refs. [23,25,26] as described above. For comparison, the constant normalization factor for the TOF data (1.033 ± 0.040) is plotted as the blue line in Fig. 9.

B. Nucleosynthesis

Among the stable Fe and Ni isotopes, ^{54}Fe and ^{58}Ni are unique because they are not produced but depleted via neutron capture, and were, therefore, proposed for constraining the neutron exposure of the weak *s* process in the He and C burning zones of massive stars [64].

The effect of the new stellar cross section on nucleosynthesis in AGB stars was investigated with stellar models of initial mass $2M_\odot$, $3M_\odot$, and $6M_\odot$ for solar metallicity ($Z = 0.014$) and roughly one tenth of solar ($Z = 0.001$). The effect of the new ^{54}Fe$(n,\gamma)^{55}$Fe cross section was tested using a 77-species network, which includes a small network around the iron group elements. For one model ($3M_\odot$, $Z = Z_{\rm solar}$) a full *s*-process network that includes species up to Po was used to test the validity of the 77-species runs. Details of the nuclear network and the numerical method employed in the postprocessing code are given in Refs. [65,66], and information on the stellar evolutionary sequences used as input into the postprocessing can be found in Refs. [67,68].

During the postprocessing we artificially included a proton profile in the He-rich intershell at the deepest extent of each dredge-up in the $2M_\odot$ and $3M_\odot$ models. The proton abundance is chosen such that it decreases exponentially from the envelope value of ~0.7 to a value of 10^{-4} at a location in mass $(2 \times 10^{-3})M_\odot$ below the base of the envelope. The protons are captured by the abundant ^{12}C in the envelope to form a region rich in ^{13}C. In between convective thermal pulses, the reaction ^{13}C$(\alpha,n)^{16}$O burns radiatively in the intershell and releases free neutrons, which are captured by Fe group isotopes including ^{54}Fe. The by-far dominant ^{13}C neutron source is complemented by the ^{22}Ne$(\alpha,n)^{25}$Mg reaction that is marginally activated by the higher temperatures of ~250 MK during the He shell flashes. In the $6M_\odot$ model we do not include any protons into the He intershell; instead neutrons are only produced by the ^{22}Ne$(\alpha,n)^{25}$Mg reaction during convective He-shell burning. The higher neutron density—owing to peak temperatures exceeding 300 MK in these—models (see, e.g., Ref. [68]) allows for the *s*-process reaction flow to bypass the branching at ^{59}Fe and to produce the radioactive ^{60}Fe.

Apart from the rate of the ^{54}Fe$(n,\gamma)^{55}$Fe reaction all the tests used the same input for the stellar and nuclear physics to compare the effect of the new cross sections presented here with that from the KADoNiS database. It turned out that the new cross section does not change the average surface composition in the winds of any of the stellar models considered. For all Fe isotopes we report changes of <1% for all stellar models. Also, none of the elements heavier than Fe (e.g., *s*-process elements such as Sr or Ba) were affected by changing the cross section of the ^{54}Fe$(n,\gamma)^{55}$Fe reaction.

Variations in the order of 1% are well within the uncertainties of the measured Fe abundances in presolar grains. Therefore, the abundances obtained by using our new MACS of ^{54}Fe are consistent with the abundances obtained by using the previous MACS from the literature.

We mentioned that the depletion of ^{54}Fe can be used to constrain the neutron exposure in stellar model calculations. The ~4% uncertainty of the MACS obtained in this work makes the use of the ^{54}Fe as a diagnostic more robust, whereas uncertainties from other nuclear reactions and from stellar physics assumptions (see, e.g., Refs. [69–71]) are now more relevant. Accordingly, to date there seems to be no need for further improvement of the ^{54}Fe(n,γ) cross section in stellar nucleosynthesis applications.

VII. SUMMARY

The neutron capture reaction ^{54}Fe$(n,\gamma)^{55}$Fe represents an excellent candidate for comparing different and independent methods for cross-section measurements. While time-of-flight-based techniques provide continuous data over a wide energy range, neutron activation of ^{54}Fe combined with AMS detection of ^{55}Fe at the VERA laboratory, where ^{55}Fe detection was demonstrated to be precise at a level of 1%, allows one to gain information on cross-section values for only a few selected neutron energies. In this way, the more complicated TOF technique can be checked and normalized with AMS data, in particular in cases of reactions with large scattering to capture ratios.

The potential of neutron activation and subsequent AMS analysis for accurate cross-section studies has been demonstrated by the present measurements at thermal and keV neutron energies. At thermal, the previously recommended value was confirmed, but with a 2.5-times reduced uncertainty. The good agreement with the results at 25 keV provides evidence for the proper treatment of strong scattering resonances in the analysis of advanced TOF measurements. It was also shown that the combination of neutron activation and AMS reached an accuracy level that is not only competitive but exceeds that of advanced TOF measurements. Accordingly, such data are of key importance for normalization of previous TOF results.

The impact of the improved cross sections for neutron capture nucleosynthesis was investigated for the case of AGB stars. Indeed, the expected depletion effect of ^{54}Fe was found to be rather weak for constraining the neutron fluence in these stars.

ACKNOWLEDGMENTS

This work was partly funded by the Austrian Science Fund (FWF), Projects No. P20434 and No. I428, and by the Australian Research Council, Project No. DP140100136. A.K. thanks Maria Lugaro for the nuclear network used to perform the *s*-process calculations. M.P. acknowledges support for NuGrid from NSF Grants No. PHY 02-16783 and No. PHY 09-22648 (Joint Institute for Nuclear Astrophysics, JINA), grants PHY-1430152 (JINA Center for the Evolution of the Elements) and EU MIRG-CT-2006-046520, and support from the "Lendület-2014" Programme of the Hungarian Academy of Sciences and from SNF (Switzerland). L.Sz. acknowledges support via the Bólyai Research Fellowship of the Hungarian Academy of Sciences and the NAP VENEUS08 (OMFB-00184/2006) project.

[1] H.-A. Synal, Int. J. Mass Spectrom. **349-350**, 192 (2013).
[2] W. Kutschera, Int. J. Mass Spectrom. **349-350**, 203 (2013).
[3] A. Wallner, Nucl. Instrum. Methods Phys. Res., Sect. B **268**, 1277 (2010).
[4] H. Nassar *et al.*, Phys. Rev. Lett. **94**, 092504 (2005).
[5] A. Wallner *et al.*, Phys. Rev. Lett. **112**, 192501 (2014).
[6] M. Heil, F. Kappeler, E. Uberseder, R. Gallino, and M. Pignatari, Phys. Rev. C **77**, 015808 (2008).
[7] F. Käppeler, R. Gallino, S. Bisterzo, and W. Aoki, Rev. Mod. Phys. **83**, 157 (2011).
[8] Z. Bao *et al.*, At. Data Nucl. Data Tables **76**, 70 (2000).
[9] I. Dillmann, R. Plag, F. Käppeler, and T. Rauscher, in *EFNUDAT Fast Neutrons—Scientific Workshop on Neutron Measurements, Theory & Applications*, edited by F.-J. Hambsch (JRC-IRMM, Geel, 2009), pp. 55–58; http://www.kadonis.org.
[10] I. Dillmann *et al.*, in *Nuclei in the Cosmos XIII*, *PoS—Proceedings of Science*, edited by Z. Fülöp (SISSA, Trieste, 2014), p. contribution 057; http://pos.sissa.it
[11] P. E. Koehler *et al.*, Phys. Rev. C **62**, 055803 (2000).
[12] P. Zugec *et al.*, Nucl. Instrum. Methods Phys. Res., Sect. A **826**, 80 (2016).
[13] C. Sneden, J. Cowan, and R. Gallino, Annu. Rev. Astron. Astrophys. **46**, 241 (2008).
[14] I. U. Roederer *et al.*, Astrophys. J. **711**, 573 (2010).
[15] C. Travaglio *et al.*, Astrophys. J. **601**, 864 (2004).
[16] R. Reifarth, C. Lederer, and F. Käppeler, J. Phys. G **41**, 053101 (2014).
[17] K. Marhas *et al.*, Astrophys. J. **689**, 622 (2008).
[18] S. Woosley, A. Heger, and T. Weaver, Rev. Mod. Phys. **74**, 1015 (2002).
[19] W. Hillebrandt and J. Niemeyer, Annu. Rev. Astron. Astrophys. **38**, 191 (2000).
[20] T. Rauscher *et al.*, Rep. Prog. Phys. **76**, 066201 (2013).
[21] M. Pignatari *et al.*, Astrophys. J. Lett. **808**, L43 (2015).
[22] H. Beer and R. Spencer, Nucl. Phys. A **240**, 29 (1975).
[23] B. Allen, A. de L. Musgrove, J. Boldeman, and R. Macklin, Australian Atomic Energy Commission, Technical report AAEC/E403 (1977).
[24] B. Allen, A. de L. Musgrove, J. Boldeman, and R. Macklin, in *Neutron Data of Structural Materials for Fast Reactors*, edited by K. Böckhoff (Pergamon Press, Oxford, 1979), p. 447.
[25] A. Brusegan *et al.*, in *Nuclear Data for Science and Technology*, edited by K. Böckhoff (ECSC, EEC, EAEC, Brussels and Luxembourg, 1983), p. 127.
[26] G. Giubrone, Ph.D. thesis, Universidad de Valencia CSIC, 2014 (unpublished); webgamma.ific.uv.es/gamma/wp-content/uploads/2014/07/PhD_GGiubrone_8July14.pdf.
[27] G. Giubrone *et al.*, Nucl. Data Sheets **119**, 117 (2014).
[28] M. Chadwick *et al.*, Nucl. Data Sheets **112**, 2887 (2011).
[29] K. Shibata *et al.*, J. Nucl. Sci. Technol. (Abingdon, UK) **48**, 1 (2011).
[30] Technical report (OECD Nuclear Energy Agency, Paris, 2014); https://www.oecd-nea.org/dbdata/jeff/.
[31] S. Mughabghab, in *Atlas of Neutron Resonances, 5th Edition* (Elsevier, Amsterdam, 2006).
[32] C. Vockenhuber, M. Bichler, A. Wallner, W. Kutschera, I. Dillmann, and F. Kappeler, Phys. Rev. C **77**, 044608 (2008).
[33] M. Berglund and M. Wieser, Pure Appl. Chem. **83**, 397 (2011).
[34] Z. Révay *et al.*, Nucl. Instrum. Methods Phys. Res., Sect. B **213**, 385 (2004).
[35] L. Szentmiklosi, T. Belgya, Zs. Révay, and Z. Kis, J. Radioanal. Nucl. Chem. **286**, 501 (2010).
[36] T. Belgya, Z. Kis, and L. Szentmiklosi, Nucl. Data Sheets **119**, 419 (2014).
[37] K. Buczak, Master's thesis, University of Vienna, 2009 (unpublished).
[38] B. Pritychenkov and S. Mughabghab, Nucl. Data Sheets **113**, 3120 (2012); Brookhaven National Laboratory Report BNL-98403-2012-JA.
[39] A. D. Carlson *et al.*, Nucl. Data Sheets **110**, 3215 (2009).
[40] A. Carlson *et al.*, Nucl. Data Sheets **118**, 126 (2014).
[41] W. Ratynski and F. Käppeler, Phys. Rev. C **37**, 595 (1988).
[42] J. Marganiec, I. Dillmann, C. Domingo-Pardo, and F. Käppeler, Phys. Rev. C **90**, 065801 (2014).
[43] J. Marganiec, I. Dillmann, C. D. Pardo, F. Kappeler, and S. Walter, Phys. Rev. C **82**, 035806 (2010).
[44] R. Reifarth, M. Heil, F. Käppeler, and R. Plag, Nucl. Instrum. Methods Phys. Res., Sect. A **608**, 139 (2009).
[45] I. Dillmann *et al.*, Nucl. Data Sheets **120**, 171 (2014).
[46] C. Massimi *et al.*, Eur. Phys. J. A **50**, 124 (2014).
[47] n_TOF Collaboration, C. Massimi, C. Domingo Pardo, and M. Calviani, Phys. Rev. C **81**, 044616 (2010).
[48] C. Lederer *et al.*, Phys. Rev. C **83**, 034608 (2011).
[49] P. Jiménez-Bonilla and J. Praena, in *Nuclei in the Cosmos XIII*, *PoS—Proceedings of Science*, edited by Z. Fülöp (SISSA, Trieste, 2015), p. contribution 102; http://pos.sissa.it.
[50] A. Carlson *et al.*, Kor. J. Nucl. Sci. Technol. **59**, 1390 (2011).
[51] H. Xiaolong and Kang Menxiao, Nucl. Data Sheets **133**, 221 (2016).
[52] W. Dixon, Nucleonics **8**, 68 (1951).
[53] NIST Technical report (2009); http://www.nist.gov/pml/data/xraycoef/index.cfm.
[54] S. K. Basu, G. Mukherjee, and A. A. Sonzogni, Nucl. Data Sheets **111**, 2555 (2010).

[55] P. Steier *et al.*, Nucl. Instrum. Methods Phys. Res., Sect. B **240**, 445 (2005).
[56] G. Korschinek, D. Mueller, T. Faestermann, A. Gillitzer, E. Nolte, and M. Paul, Nucl. Instrum. Methods Phys. Res., Sect. B **52**, 498 (1990).
[57] A. Wallner *et al.*, Nucl. Instrum. Methods Phys. Res., Sect. B **259**, 677 (2007).
[58] A. Wallner *et al.*, Nucl. Instrum. Methods Phys. Res., Sect. B **294**, 374 (2013).
[59] T. Belgya, Z. Kis, L. Szentmikl, Zs. Rvay, F. Gunsing, R. B. Firestone, and A. Wallner, *Report, IAEA Technical Meeting on the Use of Neutron Beams for High Precision Nuclear Data Measurements* (2013).
[60] W. Brooksbank, G. Leddicotte, W. Lyon, and S. Reynolds, in *Nuclear Science and Engineering Congress* (American Nucl. Scoc., Cleveland, 1955x), p. 203.
[61] H. Pomerance, Phys. Rev. **88**, 412 (1952).
[62] R. Macklin and J. Gibbons, Rev. Mod. Phys. **37**, 166 (1965).
[63] H. Beer, F. Voß, and R. Winters, Astrophys. J., Suppl. Ser. **80**, 403 (1992).
[64] S. Woosley and T. Weaver, Astrophys. J., Suppl. Ser. **101**, 181 (1995).
[65] A. Karakas and M. Lugaro, Astrophys. J. Lett. **825**, 26 (2016).
[66] A. Wallner *et al.*, Phys. Rev. C **93**, 045803 (2016).
[67] A. Karakas, Mon. Not. R. Astron. Soc. **445**, 347 (2014).
[68] C. Fishlock, A. Karakas, M. Lugaro, and D. Yong, Astrophys. J. Lett. **797**, 44 (2014).
[69] F. Käppeler *et al.*, Astrophys. J. **437**, 396 (1994).
[70] L.-S. The, M. F. El Eid, and B. S. Meyer, Astrophys. J. **655**, 1058 (2007).
[71] M. Pignatari *et al.*, Astrophys. J. **710**, 1557 (2010).